

Received July 6, 2018, accepted September 3, 2018, date of publication September 17, 2018, date of current version October 12, 2018.

Digital Object Identifier 10.1109/ACCESS.2018.2870568

Fidelity Measurement on Signal Detection Algorithms With Application to AFM Imaging

SAYAN GHOSAL¹, (Member, IEEE), AND MURTI SALAPAKA², (Senior Member, IEEE)

¹Seagate Technology, Shakopee, MN 55379, USA

²Department of Electrical and Computer Engineering, University of Minnesota, Minneapolis, MN 55455, USA

Corresponding author: Sayan Ghosal (ghos0087@umn.edu)

This work was supported in part by the USA National Science Foundation under Grant NSF-CCF 1116971 and Grant NSF-ECCS 1202411.

ABSTRACT Many signal processing and decision making algorithms reported in contemporary literature characterize the performance of the proposed methods utilizing decision error rates. However there is significant need for strategies that provide quantitative assessment of the fidelity of decisions made by the algorithms. This paper develops novel techniques utilizing which fidelity measures can be assigned quantitatively on some prevalent signal detection algorithms. The developed fidelity measurement methods with the detection algorithms are employed for topography imaging utilizing dynamic mode atomic force microscope (AFM). The AFM is a versatile metrology tool for interrogating material at the nano-scale. In spite of its remarkable achievements, a key issue that remains largely unaddressed is the assessment of fidelity of the measurement data. The developed paradigm facilitates user specific priority for either detection of sample features with high decision confidence or on not missing detection of true features. The fidelity measures presented here are suitable for real-time implementation. A detailed comparative study is presented to characterize the proposed signal detection algorithms and fidelity measurement techniques under practical AFM applications. Comprehensive simulation and experimental data corroborate the effectiveness of proposed methods.

INDEX TERMS Atomic force microscopy, detection algorithms, estimation, Kalman filters, observers, scanning probe microscopy, signal detection, signal processing algorithms.

I. INTRODUCTION

Signal processing and detection algorithms, in general, are utilized in numerous scientific applications today [1], some examples of which include but not limited to communication systems and wireless networks [2]–[4], audio signal processing [5]–[7], navigation and imaging [8]–[10] and biomedical applications [11]–[13]. Many studies reported in contemporary literature develop application specific decision making algorithms based on measurement data and characterize the algorithms in terms of decision error rates. However, quantitative assignment of fidelity measures on the decisions receives less emphasis. For example, false negative detection rate and false positive detection rates (or other parameters derived using the false negative and false positive rates) to characterize performance of algorithms are utilized for detection of features in images [9], [14], motion detection in surveillance videos [15], detection of QRS waveforms in electrocardiogram signals [16], and detecting human movements and

falls [17]–[19]. Examples of other decision making algorithms include [20], [21] where selection of the most reliable relays for secure wireless communication networks are discussed with further discussion of wireless caches in [22]–[24]. In [20]–[24], the proposed techniques are characterized in terms of symbol error rate and outage probabilities. All the examples outlined above, demonstrate effective strategies which are well suited for custom applications; however, here decision fidelity is not emphasized. Even though the references provided only a small fraction of the classification and detection literature, it is evident that there is a significant need for practical methods to assess and quantify fidelity of decisions reached. In this article, we develop methods that quantitatively estimate decision fidelity for signal detection algorithms. We then instantiate our methods for high bandwidth topography imaging using the atomic force microscope (AFM).

AFM is widely employed to explore materials at the nanometer or sub-nanometer scale. Since the invention of

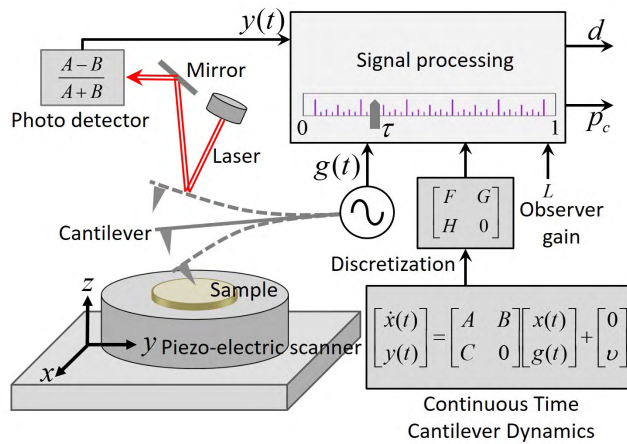


FIGURE 1. A flexible cantilever probe with a sharp tip can be moved in three spatial directions with respect to sample using a piezo-electric nano-positioner. The position of the tip is measured via a laser, photo-detector setup. In dynamic mode of AFM, the cantilever is excited with sinusoidal excitation g at or near its first mode resonant frequency. The trajectory of the oscillating cantilever changes depending on the intermittent tip-sample interactions. For fast dynamic mode imaging, the measured deflection y and excitation g are input to a signal processing block. The continuous time dynamics of the cantilever represented by state-space matrices (A, B, C) is measured away from sample which is utilized to obtain a discrete time dynamical model specified by the matrices (F, G, H) . The signal processing unit utilizes different detection algorithms, the discrete time cantilever dynamics and a Kalman observer with gain L to generate likelihood ratio signals. The adjustable threshold τ controls the balance between false alarm and missed detection rates by the decision signal d on the presence or absence of topographic features. Further, fidelity signal p_c assigns confidence measures on the decision signals.

the AFM [25], researchers have developed a diverse set of AFM based measurement techniques with significant impact on science and technology. For example, structure of a single pentacene molecule is revealed by AFM in [26], AFM techniques are utilized to realize data storage solutions [27] with ultra-high densities (more than 5 Tb/in^2) [28], high speed AFM imaging scheme suitable for video rate imaging of biological motors is reported in [29] and mechanical properties of interesting polymer and biological samples are investigated in [30]–[34]. Apart from imaging, AFMs are also the preferred instruments for force spectroscopy measurements on single protein molecules [35], [36]. A detailed set of applications where AFMs are used can be found in [37] and [38].

The principal component of the AFM is a flexible cantilever probe which can be moved in x - y - z directions with respect to the sample surface by a piezo-electric actuator (see Fig. 1). The cantilever has a sharp tip at one end. The atoms on the tip experience forces when in close proximity to atoms on the sample surface. The interatomic tip-sample forces deflect the cantilever which is measured by a laser-photodiode setup. In traditional contact mode operation, the cantilever is scanned over the sample surface in the x - y plane where the cantilever deflection is regulated at a desired set point by actuating the z -positioner. The vertical movement of the z -positioner used to regulate constant

deflection of the cantilever is interpreted as the sample topography. In the contact mode of operation, considerable wear and tear is possible for both the tip and the sample [39]. In the dynamic mode of operation, the cantilever is sinusoidally excited at or near its first resonant frequency (see Fig. 1). Unlike the traditional contact mode operation where the AFM probe is in continuous contact with sample, in the dynamic mode the oscillating cantilever interacts with the sample intermittently only during a very small fraction of its entire orbit. The interactive forces between tip and sample caused by gentle tapping of the sample surface change the orbit of the oscillating cantilever. These changes include alteration of the amplitude of oscillation and the phase of oscillation with respect to the drive, which are utilized for interpreting the topography and other features of the sample. Due to small duration of interaction between the tip and sample, the dynamic mode operation results in minimal mechanical wear of the probe and sample material [40].

In spite of the wide spectrum of applications, in the dynamic mode, quantitative interpretation of the AFM data becomes challenging due to complex trajectories of AFM probe [32], [37], [41]. A natural question that arises in this context is the assessment of the *goodness* of the inferences drawn from AFM measurement data. Such emphasis on quantitative assessment of the quality of measurement data with error bounds is a standard practice in most instruments used for metrology. However, there is a lack of tools that quantify fidelity measures on the AFM measurements in real-time. Determining fidelity measures for AFM in general is a challenging problem. In this article, a real time method is reported to quantify fidelity of AFM measurements obtained using the dynamic mode operation [42], [43].

In related works [27], [44]–[48], observer based architectures [49] are utilized to achieve detection of topographic features at high bandwidth. There, the tracking error generated by the observer is matched to a linear time-invariant model of the cantilever dynamics to generate a likelihood ratio based signal. The likelihood ratio based signal is compared to a user defined threshold (denoted as τ in Fig. 1) to decide presence or absence of topographic features [50]. With the methods developed in this article it becomes possible for the decision image (shown as d in Fig. 1) that shows absence or presence of a topographic feature at any pixel to be accompanied by a fidelity image (shown as p_c in Fig. 1). The fidelity image assigns a quantified measure of confidence on the decision reached at each pixel. The fidelity image accompanying the decision image is a function of choice of threshold selected by user. The user can prioritize detection of most true features by setting a low threshold or can emphasize that most features detected are true features by selecting a high threshold. Such facility is particularly suitable for a two step exploration process; in the first step the user can obtain a quick overview of a large area of the sample for identifying/detecting regions that are promising for finer investigation. Here the user can set a low threshold that will help pruning out uninteresting areas. The first exploratory

step can be performed at high speeds thereby facilitating rapid pruning of areas with no features. This step can be followed by finer investigation of the areas which are left unpruned. For the second step a high threshold can be chosen to ensure that detected features are true features with high probability. We remark that often the image sought occupies a small fraction of the entire sample area (see Fig. 5 in [46] that shows an image of a DNA obtained by an AFM with a height of 1.5 nm where the DNA strand occupies only a small fraction of the image). Thus the pruning step can identify the small region of interest which can be investigated with more attention.

Fidelity measurement for AFM was first introduced by the authors in a letter [45]. The present article provides a detailed analysis of false alarm, missed detection rate and performance of the methods which were not studied before. A quantitative comparison of different imaging methods, namely the locally most powerful (LMP) [1], [51] and the generalized likelihood ratio test (GLRT) based method [1], [51] (described in detail later) with respect to threshold selection is presented. An alternative detection scheme developed and adopted in this article is referred to as the modified generalized likelihood ratio test (MGLRT) method. It is demonstrated that LMP based method is less sensitive to threshold selection compared to GLRT followed by MGLRT. However, as demonstrated by experiments, the MGLRT based method is well suited for real-time implementation in practical AFM usage. To summarize, the key contributions of this article are:

- Development of the simple MGLRT method for real time fidelity imaging with applications to dynamic mode AFM
- Detailed analytical derivation of the detection performance for different imaging methods, namely, the LMP, GLRT and MGLRT methods
- Analytical derivation of fidelity measures for the MGLRT and GLRT techniques
- Extensive comparison and verification of the LMP, GLRT and MGLRT schemes based on simulation and experimental data for AFM imaging application. Further discussions on practical challenges are also presented.

It is discussed before that fidelity measurement, in general, is still widely unaddressed by many researchers working on diverse applications of signal processing, detection and classification algorithms. Thus the techniques developed in this article, although are employed specifically to AFM imaging, hold the promise to find broader set of applications as well.

This article is organized as follows: Section II briefly introduces the observer based architecture for fast dynamic mode AFM imaging. Section III develops and analyzes the false alarm rate, detection probability and fidelity metrics as a function of decision threshold. Section IV verifies the analytical methods for fidelity imaging using realistic simulation models of the AFM setup. Section V demonstrates the efficacy of proposed methods using experimental results. Section VI concludes this work.

II. PRELIMINARIES

We now provide the problem description in terms of the AFM application which will also serve to motivate the analytical abstraction used in the subsequent sections. We first describe observer based dynamic mode AFM imaging methodology. The first mode approximation of the cantilever is governed by the dynamics

$$\ddot{p} + \frac{\omega_0}{Q}\dot{p} + \omega_0^2 p = f(t) = \frac{1}{m}(g + h), \quad (1)$$

$$h = \phi(p, \dot{p}), \quad y = p + v, \quad (2)$$

where p and \dot{p} are the deflection and velocity of the cantilever at the tip location respectively. m is the mass of the lever. The total force per unit mass, $f(t)$, depends on the dither excitation input g and the nonlinear interactive force h between cantilever tip and sample. Typically, g is chosen to be sinusoidal with frequency close to the resonant frequency ω_0 . Q is the quality factor. ω_0 and Q can be determined from a frequency sweep method when the cantilever is free from sample. y is the measured deflection and v is the measurement noise. Equation (1) can be represented in state space form described by

$$\dot{x} = Ax + Bf, \quad y = Cx + v, \quad (3)$$

where the state is defined by $x = [p \ \dot{p}]^T$ with the matrices $A = [0 \ 1; -\omega_0^2 \ -\frac{\omega_0}{Q}]$, $B = [0 \ 1]^T$ and $C = [1 \ 0]$. In the dynamic mode of operation where the cantilever is excited by sinusoidal forcing g , the cantilever typically oscillates with a steady state amplitude ranging between 25 nm to 200 nm. The interaction with the sample occurs only during a very small fraction of cantilever orbit. Thus the force h between tip and sample can be modeled as an impulsive force exerted by the sample on the tip when the tip is closest to the sample while oscillating. The impulsive force changes the cantilever state modeled as an instantaneous change. A discrete time model for cantilever dynamics with such impulsive interaction model can be written as [46]

$$x_{k+1} = Fx_k + Gg_k + \delta_{\theta, k+1}v, \quad (4)$$

$$y_k = Hx_k + v_k,$$

where k denotes the index for discrete time. The matrices F , G and H can be obtained from continuous time model (3) by discretization. $\delta_{\theta, k+1}v$ denotes the sudden change in the state at the time of impact. v denotes the strength of impulsive interaction and θ models the time of impact ($\delta_{i,j} = 1$ when $i = j$, else 0). A fast AFM imaging technique developed in [46] uses Kalman observer [49] for generating test signals. The Kalman observer is matched to the discrete time cantilever model described in (4). Here, let \hat{x}_k be the estimated state from Kalman observer with observer gain L which follows the dynamics

$$\hat{x}_{k+1} = F\hat{x}_k + Gg_k + L(y_k - H\hat{x}_k), \quad (5)$$

$$\hat{y}_k = H\hat{x}_k, \quad e_k = (y_k - \hat{y}_k).$$

From (4) and (5) it follows that, after an impact at time θ , e_k can be written as (see [46])

$$e_k = \Gamma_{k;\theta} v + \eta_k; \quad \Gamma_{k;\theta} := H(F - LH)^{k-\theta}, \quad (6)$$

where η_k is zero mean Gaussian noise with variance σ_η^2 . $\Gamma_{k;\theta}$ denotes the impulse response for the system that maps force input to the error signal e_k . Let M be the window size chosen for detection purposes. The binary hypotheses;

$$H_0 : e_k = \eta_k, \quad H_1 : e_k = \Gamma_{k;\theta} v + \eta_k, \quad (7)$$

represent absence and presence of sample with $k = 1, 2, \dots, M$. Let

$$\Gamma := [H, H(F - LH), \dots, H(F - LH)^{M-1}]^T, \quad (8)$$

and the observation vector $e := [e_1, e_2, \dots, e_M]^T$. Assuming the impact time $\theta = 1$, the hypotheses can be expressed in the form

$$H_0 : e = \eta, \quad H_1 : e = \Gamma v + \eta, \quad (9)$$

where η denotes the zero mean Gaussian noise vector $[\eta_1, \eta_2, \dots, \eta_M]$ with covariance matrix $V = \sigma_\eta^2 I$, I is identity matrix of size $M \times M$. The test vector e can be processed using either locally most powerful or generalized likelihood ratio techniques for which fidelity metrics are determined below.

III. DECISION THRESHOLDS AND FIDELITY METRICS

The problem described by (8) and (9) with statistics of noise given by V is a general model that can be applied to numerous applications. In this section we quantify fidelity in terms of decision thresholds. The locally most powerful (LMP) and generalized likelihood ratio test (GLRT) methods [1], [52] are utilized to process the tracking error e_k for detection purposes. An alternative detection method is also adopted in this article which is referred to as the modified generalized likelihood ratio test (MGLRT) method. These methods yield likelihood ratios that are compared with respect to user defined thresholds for deciphering presence or absence of sample. The probability of false alarm (P_{FA}) is defined to be the probability that the user decides that hypothesis H_1 is true incorrectly where the sample is absent. The probability of detection P_D is defined to be the probability that the user correctly decides hypothesis H_1 in presence of the sample. The decision threshold τ set by the user yields a trade-off between the false alarm rate P_{FA} and probability of missed detection $1 - P_D$. Fidelity metrics, P_{FA} and P_D for GLRT, MGLRT and LMP techniques are developed below.

A. FIDELITY AND THRESHOLD SELECTION FOR GLRT, MGLRT AND LMP IMAGING

The likelihood ratio test signal for LMP technique is defined as $l_{lmp} := e^T V^{-1} \Gamma$ where V represents covariance matrix of noise and Γ is defined in (8). Both Γ and V can be determined

from experimental data. Thus, under the hypotheses H_0 and H_1 , the likelihood test signal evaluates as follows:

$$\begin{aligned} H_0 : l_{lmp} &= \eta^T V^{-1} \Gamma, \\ H_1 : l_{lmp} &= v \Gamma^T V^{-1} \Gamma + \eta^T V^{-1} \Gamma. \end{aligned} \quad (10)$$

Let $p_{lmp}(l_{lmp}; H_0)$ denote the probability density function (pdf) of l_{lmp} under hypothesis H_0 . Notice in (10) that under H_1 , the pdf of l_{lmp} depends on v . v depends on the strength of interactive forces between cantilever tip and sample; it is assumed that v follows a distribution $p(v)$. Let $p_{lmp}(l_{lmp}; H_1, v)$ denote the conditional pdf of l_{lmp} under hypothesis H_1 given a specific value v . Since η represents a zero mean Gaussian random vector, it follows that $p_{lmp}(l_{lmp}; H_0) \sim \mathcal{N}(0, \sigma_{lmp}^2)$ and $p_{lmp}(l_{lmp}; H_1, v) \sim \mathcal{N}(\mu_{lmp}(v), \sigma_{lmp}^2)$ with $\sigma_{lmp} = \sqrt{\Gamma^T V^{-1} \Gamma}$ and $\mu_{lmp}(v) = v \Gamma^T V^{-1} \Gamma$. $\mathcal{N}(\mu, \sigma^2)$ represents standard Gaussian distribution with mean μ and variance σ^2 . For LMP based hypothesis testing framework it follows that:

$$P_{FA} = \int_{\tau_{lmp}}^{\infty} p_{lmp}(y; H_0) dy = Q\left(\frac{\tau_{lmp}}{\sigma_{lmp}}\right), \quad (11)$$

where $Q(x) := \frac{1}{\sqrt{2\pi}} \int_x^{\infty} e^{-y^2/2} dy$. The probability of detection P_D for LMP test can be evaluated as:

$$\begin{aligned} P_D &= \int_{\tau_{lmp}}^{\infty} p_{lmp}(y; H_1) dy \\ &= \int_{\tau_{lmp}}^{\infty} \int_{-\infty}^{\infty} p_{lmp}(y; H_1, v) p(v) dv dy \\ &= \int_{-\infty}^{\infty} Q\left(\frac{\tau_{lmp} - \mu_{lmp}(v)}{\sigma_{lmp}}\right) p(v) dv. \end{aligned} \quad (12)$$

Further, the likelihood ratio test signal for GLRT technique is given by $l_{glrt} := e^T V_{\Gamma, glrt} e$ with $V_{\Gamma, glrt} = V^{-1} \Gamma \Gamma^T V^{-1}$. From the definition $l_{glrt} := e^T V_{\Gamma, glrt} e$ it can be shown that, $l_{glrt} = l_{lmp}^2$ where l_{lmp} is scalar. Since l_{lmp} follows Gaussian distribution under hypothesis H_0 , it can be shown that for GLRT test, under H_0 :

$$p_{glrt}(l_{glrt}; H_0) = \frac{1}{\sqrt{2\pi V_{\Gamma} l_{glrt}}} e^{-\frac{l_{glrt}}{2V_{\Gamma}}}, \quad (13)$$

where $V_{\Gamma} = \Gamma^T V^{-1} \Gamma$. Further, it follows that under H_1 :

$$p_{glrt}(l_{glrt}; H_1, v) = \frac{1}{\sqrt{2\pi V_{\Gamma} l_{glrt}}} e^{-\frac{l_{glrt} + v^2 V_{\Gamma}^2}{2V_{\Gamma}}} \cosh(v \sqrt{l_{glrt}}). \quad (14)$$

Let τ_{glrt} be the decision threshold for GLRT test. Then it follows that the probability of false alarm:

$$P_{FA} = P(\text{Decision is } H_1 | H_0) = \int_{\tau_{glrt}}^{\infty} p_{glrt}(y; H_0) dy. \quad (15)$$

Further, the probability of detection for GLRT test is given by:

$$\begin{aligned} P_D &= P(\text{Decision is } H_1 | H_1) \\ &= \int_{\tau_{glrt}}^{\infty} \int_{-\infty}^{\infty} p_{glrt}(y; H_1, v) p(v) dv. \end{aligned} \quad (16)$$

Thus the false alarm rate and probability of detection for the GLRT scheme can be determined numerically using (15) and (16) where $p_{glrt}(l_{glrt}; H_0)$ and $p_{glrt}(l_{glrt}; H_1, \nu)$ are given by (13) and (14) respectively. Note that, evaluation of the expressions (12) and (16) requires that the distribution of the impulsive forces between the tip and sample $p(\nu)$ is known. The distribution of $p(\nu)$ can be estimated by gathering least square estimates of ν (denoted by $\hat{\nu}$) which is described in [45]. The set of $\hat{\nu}$ when utilized for inferring statistical properties of ν reveals that the distribution $p(\nu)$ is mostly populated around a peak value with decaying tails on both sides. It is shown here that such distribution of $p(\nu)$ can be approximated using a Gaussian distribution $p(\nu) \sim \mathcal{N}(\nu_0, \sigma_\nu^2)$ (see Section IV and Section V for details).

For the GLRT technique, the matrix $V_{\Gamma, glrt}$ needs to be aligned with the observation signal e_k during each decision window to generate the likelihood ratio $l_{glrt} = e^T V_{\Gamma, glrt} e$. For LMP imaging, the matrix $V^{-1}\Gamma$ must be aligned with the observation signal e_k to generate $l_{lmp} = e^T V^{-1}\Gamma$. Thus, implementation of the LMP and GLRT techniques in practice requires additional measures for synchronization of multiplication of the matrices $V^{-1}\Gamma$ and $V_{\Gamma, glrt}$ with the observation signal e_k . For AFM experimental setups, it is challenging to extract the exact timing instant where the cantilever interacts impulsively with the sample.

Alternatively, define the test signal $l_m := e^T e$ which is referred to as the modified generalized likelihood ratio test (MGLRT) technique in this article. The MGLRT method is simpler for real time implementation in AFM setups. Here, no additional measures are needed for aligning the matrix $V_{\Gamma, glrt}$ with e_k . The test signal l_m performs well for detecting sample features [46]. Hence, in the results section we compare the LMP imaging method mostly with the MGLRT technique instead of the GLRT scheme. Under hypotheses H_0 and H_1 , for MGLRT scheme, it follows that

$$\begin{aligned} H_0 : l_m &= \eta^T \eta \\ H_1 : l_m &= (\nu \Gamma + \eta)^T (\nu \Gamma + \eta). \end{aligned} \quad (17)$$

Under H_0 , $l_m = \eta^T \eta = \sum_{i=1}^M \eta_i^2$ where each η_i (M is the size of detection window) is independent, zero mean Gaussian random variable with variance σ_η^2 . It can be shown that l_m obeys a Chi-square distribution given by:

$$p_m(l_m; H_0) = \frac{1}{\sigma_\eta^M 2^{M/2} \Gamma(M/2)} l_m^{(M/2)-1} e^{-\frac{l_m}{2\sigma_\eta^2}}, \quad l \geq 0, \quad (18)$$

where $\Upsilon(\cdot)$ denotes the standard Gamma function. Suppose that τ_m is the decision threshold. Probability of false alarm P_{FA} can be calculated analytically in the form of a finite series for even M as below:

$$\begin{aligned} P_{FA} &= \int_{\tau_m}^{\infty} p_m(l; H_0) dl \\ &= 1 - \int_0^{\tau_m} \frac{l^{M/2-1} e^{-\frac{l}{2\sigma_\eta^2}}}{\sigma_\eta^M 2^{M/2} \Gamma(M/2)} dl \\ &= e^{-\frac{\tau_m}{2\sigma_\eta^2}} \sum_{k=0}^{M/2-1} \frac{1}{k!} \left(\frac{\tau_m}{2\sigma_\eta^2} \right)^k, \quad M \text{ is even.} \end{aligned} \quad (19)$$

From (17), under hypothesis H_1 , $l_m = e^T e = (\nu \Gamma^T + \eta^T)(\nu \Gamma + \eta)$. Define $\eta' = \nu \Gamma + \eta = [\eta'_1, \eta'_2, \dots, \eta'_M]$. Given a specific value for ν it follows that each $\eta'_i, i \in \{1, 2, \dots, M\}$ is a Gaussian random variable with mean $\nu \Gamma_i$ ($\Gamma_i := H(F - LH)^{i-1}$) and variance σ_η^2 . Thus $l_m = \sum_{i=1}^M (\eta'_i)^2$ follows a non central Chi-square distribution [1] with pdf given by:

$$p_m(l_m; H_1, \nu) = \frac{1}{2\sigma_\eta^2} \left(\frac{l_m}{s^2} \right)^{\frac{M-2}{4}} e^{-\frac{s^2+l_m}{2\sigma_\eta^2}} I_{M/2-1} \left(\frac{\sqrt{l_m} s}{\sigma_\eta^2} \right), \quad (20)$$

where $s^2 = \sum_{i=1}^M \nu^2 \Gamma_i^2 = \nu^2 \Gamma^T \Gamma$. $I_\alpha(x)$ is the α^{th} order modified Bessel function of the first kind which can be represented by the infinite series $I_\alpha(x) = \sum_{k=0}^{\infty} \frac{(x/2)^{\alpha+2k}}{k! \Upsilon(\alpha+k+1)}$, $x \geq 0$. It should be noted that $I_\alpha(x)$ can be numerically evaluated quickly using its infinite series expression only when the magnitude $|x|$ is small. However for general evaluations, alternative methods are investigated in literature which achieve quicker convergence of $I_\alpha(x)$. Examples of such study include backward recurrence methods [53], Hadamard series methods [54], asymptotic series methods [55] and also the exp-arc integral based techniques [56]. Thus the probability of detection P_D can be determined using

$$\begin{aligned} P_D &= \int_{\tau_m}^{\infty} \int_{-\infty}^{\infty} p_m(l; H_1, \nu) p(\nu) d\nu dl \\ &= \int_{\tau_m}^{\infty} \int_{-\infty}^{\infty} \frac{1}{\sqrt{8\pi} \sigma_\eta^2 \sigma_\nu} \left(\frac{l}{\nu^2 \Gamma^T \Gamma} \right)^{(M-2)/4} \\ &\quad \times I_{M/2-1} \left(\frac{\sqrt{l} s}{\sigma_\eta^2} \right) e^{-\left(\frac{\nu^2 \Gamma^T \Gamma + l}{2\sigma_\eta^2} + \frac{(\nu - \nu_0)^2}{2\sigma_\nu^2} \right)} d\nu dl. \end{aligned} \quad (21)$$

The last step in (21) follows from the Gaussian assumption on the distribution $p(\nu)$.

The decision *fidelity* is defined by the conditional probability that the decision is correct given l_0 is an outcome of the random variable l_m which is denoted by $P(\text{Correct decision} | l_m = l_0)$. We consider two cases. Case 1 is given by the condition $l_0 > \tau_m$ where the decision is reached that hypothesis H_1 holds. Fidelity for case 1 is denoted by $P(H_1 | l_m = l_0, l_0 > \tau_m)$. Case 2 is specified by $l_0 \leq \tau_m$ where the decision is reached that hypothesis H_0 holds. Fidelity for case 2 is denoted by $P(H_0 | l_m = l_0, l_0 \leq \tau_m)$. The following theorem presents the methods for evaluating the fidelity measures:

Theorem 1: For the MGLRT method:

$$\begin{aligned} P(H_1 | l_m = l_0, l_0 > \tau_m) &= \frac{\alpha(l_0) \int_{-\infty}^{\infty} e^{-\frac{s^2}{2\sigma_\eta^2}} I_{M/2-1} \left(\frac{\sqrt{l_0} s}{\sigma_\eta^2} \right) p(\nu) d\nu}{1 + \alpha(l_0) \int_{-\infty}^{\infty} e^{-\frac{s^2}{2\sigma_\eta^2}} I_{M/2-1} \left(\frac{\sqrt{l_0} s}{\sigma_\eta^2} \right) p(\nu) d\nu} \end{aligned} \quad (22)$$

and

$$P(H_0|l_m = l_0, l_0 \leq \tau_m) = \frac{1}{1 + \alpha(l_0) \int_{-\infty}^{\infty} e^{-\frac{s^2}{2\sigma_\eta^2}} I_{M/2-1} \left(\frac{\sqrt{l_0}s}{\sigma_\eta^2} \right) p(v) dv}, \quad (23)$$

with $\alpha(l_0) := \sigma_\eta^{M-2} 2^{\frac{M}{2}} \Upsilon(M/2) l_0^{-\frac{M-2}{4}}$. Further, if $p(v) = \delta(v - v_0)$ where δ denotes the Dirac delta function then

$$P(H_1|l_m = l_0, l_0 > \tau_m) = \frac{\alpha(l_0) e^{-\frac{s_0^2}{2\sigma_\eta^2}} I_{M/2-1} \left(\frac{\sqrt{l_0}s_0}{\sigma_\eta^2} \right)}{1 + \alpha(l_0) e^{-\frac{s_0^2}{2\sigma_\eta^2}} I_{M/2-1} \left(\frac{\sqrt{l_0}s_0}{\sigma_\eta^2} \right)} \quad (24)$$

and

$$P(H_0|l_m = l_0, l_0 \leq \tau_m) = \frac{1}{1 + \alpha(l_0) e^{-\frac{s_0^2}{2\sigma_\eta^2}} I_{M/2-1} \left(\frac{\sqrt{l_0}s_0}{\sigma_\eta^2} \right)} \quad (25)$$

where $s_0^2 = v_0^2 \Gamma^T \Gamma$.

Proof: It follows that

$$\begin{aligned} P(\text{Correct decision}|l_m = l_0, l_0 > \tau_m) \\ &= P(H_1|l_m = l_0, l_0 > \tau_m) \\ &= \lim_{\epsilon \rightarrow 0^+} P\left(H_1|l_m \in [l_0 - \frac{\epsilon}{2}, l_0 + \frac{\epsilon}{2}], l_0 > \tau_m\right) \\ &= \lim_{\epsilon \rightarrow 0^+} \frac{\mathcal{P}_{H_1}(l_0, \epsilon) P(H_1)}{\sum_{j=0,1} \mathcal{P}_{H_j}(l_0, \epsilon) P(H_j)}, \end{aligned} \quad (26)$$

where $P(H_1)$ and $P(H_0)$ are a priori probabilities for hypotheses H_1 and H_0 . The last step in the r.h.s of (26) follows using Bayes' rule with $\mathcal{P}_{H_j}(l_0, \epsilon)$, $j \in \{0, 1\}$ defined by $\mathcal{P}_{H_j}(l_0, \epsilon) := P(l_m \in [l_0 - \frac{\epsilon}{2}, l_0 + \frac{\epsilon}{2}], l_0 > \tau_m | H_j)$. The individual terms in the numerator and the denominator of (26) can be simplified for small ϵ as:

$$\begin{aligned} \mathcal{P}_{H_1}(l_0, \epsilon) &:= \int_{-\infty}^{\infty} \int_{l_0 - \epsilon/2}^{l_0 + \epsilon/2} p_m(l; H_1, v) p(v) dl dv \\ &\approx \frac{\epsilon}{2\sigma_\eta^2} \int_{-\infty}^{\infty} \left(\frac{l_0}{s^2} \right)^{\frac{M-2}{4}} \\ &\quad \times e^{-\frac{s^2 + l_0}{2\sigma_\eta^2}} I_{M/2-1} \left(\frac{\sqrt{l_0}s}{\sigma_\eta^2} \right) p(v) dv, \end{aligned} \quad (27)$$

where $s^2 = v^2 \Gamma^T \Gamma$. Similarly,

$$\begin{aligned} \mathcal{P}_{H_0}(l_0, \epsilon) &:= \int_{l_0 - \epsilon/2}^{l_0 + \epsilon/2} p_m(l; H_0) dl \\ &\approx \frac{\epsilon}{\sigma_\eta^M 2^{M/2} \Upsilon(M/2)} l_0^{(\frac{M}{2}-1)} e^{-\frac{l_0}{2\sigma_\eta^2}}. \end{aligned} \quad (28)$$

In the limit $\epsilon \rightarrow 0^+$, the approximations in (27) and (28) can be replaced with equalities. Thus it follows that:

$$\begin{aligned} P(H_1|l_m = l_0, l_0 > \tau_m) \\ &= \frac{\alpha(l_0) \frac{P(H_1)}{P(H_0)} \int_{-\infty}^{\infty} e^{-\frac{s^2}{2\sigma_\eta^2}} I_{M/2-1} \left(\frac{\sqrt{l_0}s}{\sigma_\eta^2} \right) p(v) dv}{1 + \alpha(l_0) \frac{P(H_1)}{P(H_0)} \int_{-\infty}^{\infty} e^{-\frac{s^2}{2\sigma_\eta^2}} I_{M/2-1} \left(\frac{\sqrt{l_0}s}{\sigma_\eta^2} \right) p(v) dv}, \end{aligned} \quad (29)$$

where $\alpha(l_0) = \sigma_\eta^{M-2} 2^{\frac{M}{2}} \Upsilon(M/2) l_0^{-\frac{M-2}{4}}$

Evaluating (29) requires the a priori probabilities of the hypotheses which are $P(H_1)$ and $P(H_0)$. If the sample under study is not known a priori then it is reasonable to assume that there is equal possibility to encounter both presence and absence of sample features while imaging. Thus the hypotheses H_1 and H_0 have equal a priori probabilities. Enforcing $P(H_1) = P(H_0)$ in (29) it follows that,

$$\begin{aligned} P(H_1|l_m = l_0, l_0 > \tau_m) \\ &= \frac{\alpha(l_0) \int_{-\infty}^{\infty} e^{-\frac{s^2}{2\sigma_\eta^2}} I_{M/2-1} \left(\frac{\sqrt{l_0}s}{\sigma_\eta^2} \right) p(v) dv}{1 + \alpha(l_0) \int_{-\infty}^{\infty} e^{-\frac{s^2}{2\sigma_\eta^2}} I_{M/2-1} \left(\frac{\sqrt{l_0}s}{\sigma_\eta^2} \right) p(v) dv}. \end{aligned} \quad (30)$$

Similarly, it can be shown that:

$$\begin{aligned} P(H_0|l_m = l_0, l_0 \leq \tau_m) \\ &= \frac{1}{1 + \alpha(l_0) \int_{-\infty}^{\infty} e^{-\frac{s^2}{2\sigma_\eta^2}} I_{M/2-1} \left(\frac{\sqrt{l_0}s}{\sigma_\eta^2} \right) p(v) dv}. \end{aligned} \quad (31)$$

Alternatively assume that v follows a degenerate distribution, that is $p(v) = \delta(v - v_0)$ where δ denotes the Dirac delta function. Then (24) and (25) can be derived immediately from (30) and (31), which completes the proof. ■

Fidelity metrics for GLRT method can be evaluated in a similar fashion, for example, assuming degenerate distribution of v it can be shown that

$$\begin{aligned} P(H_1|l_{glrt} = l_0, l_0 > \tau) &= \frac{e^{-\frac{v_0^2}{2}} \cosh(v_0 \sqrt{l_0})}{1 + e^{-\frac{v_0^2}{2}} \cosh(v_0 \sqrt{l_0})}, \\ P(H_0|l_{glrt} = l_0, l_0 \leq \tau) &= \frac{1}{1 + e^{-\frac{v_0^2}{2}} \cosh(v_0 \sqrt{l_0})}. \end{aligned} \quad (32)$$

Further, fidelity metrics for LMP imaging methods are shown in [45].

B. EASE OF IMPLEMENTATION AND SIMPLIFICATIONS

Notice that for the Gaussian distribution assumption on $p(v)$, it is necessary to evaluate both v_0 and σ_v for determining fidelity metrics in (22) and (23). An average of recent estimates of v can be used as estimate of v_0 whereas standard deviation of the estimates of v can be utilized to estimate σ_v .

It is shown in [45] that a least square estimate for ν works well which is given by:

$$\hat{\nu} = (\Gamma^T \Gamma)^{-1} \Gamma^T e. \quad (33)$$

For the purpose of evaluating the false alarm rate P_{FA} using the set of equations (11), (15) and (19), and probability of detection P_D in (12), (21) and (21), the true topographic features are assumed to be known a priori. Here, $\hat{\nu}$ is evaluated using (33) at the end of each decision window of size M . The set of observations $\hat{\nu}$ gathered this way is utilized for acquiring the probability distribution of ν denoted by $p(\nu)$ which is used for determining P_D . However, in case of determining the fidelity metrics, the true topographic features are not known a priori. Thus $\hat{\nu}$ values are gathered only during the decision windows when the decision is H_1 . The latest ensemble of such estimates $\hat{\nu}$ is used to determine the probability distribution, $p(\nu)$, which is used in (22) and (23) for fidelity measures. For the LMP technique, the Gaussian assumption allows for solutions of the decision fidelity in closed analytical form [45]. However, for the MGLRT method, Gaussian assumption leads to (22) and (23) in which the integration of the form $\int_{-\infty}^{\infty} p_m(l_0; H_1, \nu) p(\nu) d\nu$ must be evaluated numerically at each decision window. Thus a real time implementation is more challenging. However, note that with the degeneracy assumption to determine fidelity metrics using (24) and (25), only the estimate of ν_0 is required. Furthermore, GLRT, MGLRT and LMP fidelity metrics can be computed using closed form analytical formulas. Hence the degeneracy approximation simplifies computation of the fidelity metrics. Note that the development in this and the previous section is applicable in a general setting. We now demonstrate in the subsequent sections that despite the simplification, the fidelity metrics remain effective for practical purposes as verified by simulation and experimental data for AFM images.

IV. SIMULATION RESULTS

The trajectory $p(t)$ of the oscillating cantilever interacting intermittently with sample in the dynamic mode operation is simulated using a piecewise linear model for the interactive forces between cantilever tip and sample [30], [57]. Such a model encapsulates many experimentally observed phenomena [58]. The topography of the sample is shown in Fig. 2 (a). The bright zones represent high topography whereas the dark zones correspond to depressed topography. The difference between high and low topography levels is 4 nm. The frequency response of an AC240TS cantilever from Asylum Research [59] is estimated where the resonant frequency f_0 and quality factor Q are found to be 71.2 kHz and 164.2 respectively. The continuous time state space model in (3) is derived from the frequency response which in turn is utilized for simulation. The excitation frequency is matched to f_0 and the oscillation amplitude (free from tip-sample interaction) is 30 nm. Further, the discrete time dynamics in (4) is determined from the continuous time model via zero order

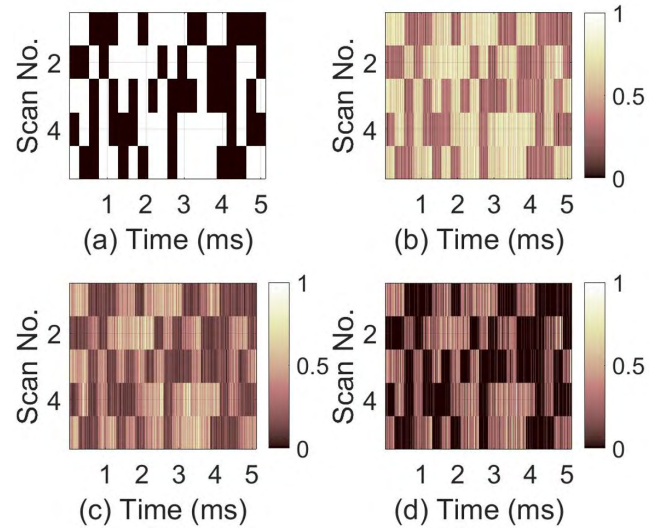


FIGURE 2. (Simulation result) (a) Height image. Bright zones represent high topography while dark zones represent low topography. The difference between low and high topography is 4 nm. (b) LMP likelihood image, (c) MGLRT likelihood image and (d) GLRT likelihood image. x axis represents time in the unit of milliseconds. y axis represents index of scan line. Both LMP, MGLRT and GLRT images are normalized with respect to corresponding maximum values. The color bars specify the ranges.

hold discretization at sampling frequency of 2 MHz [60]. A steady state Kalman observer with gain L shown in (5) is designed to match the discrete time model. The discrete time measurement noise ν_k in (4) is chosen to be zero mean with standard deviation σ_ν such that the noise bed is retained within 100 pm ($3\sigma_\nu < 100$ pm) which is normally observed in our experimental data. $\sigma_\nu^2 = 0.5 \times 10^{-3} \text{ nm}^2$ satisfies this criteria. The steady state variance σ_η^2 of the noise η_k present in the tracking error in (6) can be determined by solving the discrete time algebraic Riccati equation for the covariance matrix of the state estimation error of the observer in (5) [61]. The window size M for hypothesis testing in (7) is chosen to be 20 samples. The Γ vector in the hypothesis testing framework (9) is determined as explained in Section II. LMP, MGLRT and GLRT likelihood ratios l_{lmp} , l_m and l_{glrt} are synthesized from the tracking error e which are shown in Fig. 2 (b), Fig. 2 (c) and Fig. 2 (d) respectively.

Statistics for the strength of interaction between cantilever tip and sample ν is obtained by gathering the estimates $\hat{\nu}$ using (33) (shown in Fig. 3). Fig. 3 demonstrates that the histogram of $\hat{\nu}$ exhibits a peak with tails extending on both sides. For simple calculation of the false alarm and detection probabilities, the histogram in Fig. 3 (b) can be fit approximately with a Gaussian distribution of mean $\nu_0 = 0.57$ and standard deviation $\sigma_\nu = 0.152$. For finer precision, the distribution can be represented in a table form and used directly for numerical evaluation of the detection and false alarm probabilities. For simple evaluation of fidelity metrics using the degenerate assumption of $p(\nu)$ as explained in Section III-B, the peak of the distribution ν_0 estimated by the Gaussian fit serves reasonably well which is demonstrated by simulation in this section and by experimental results in the next section.

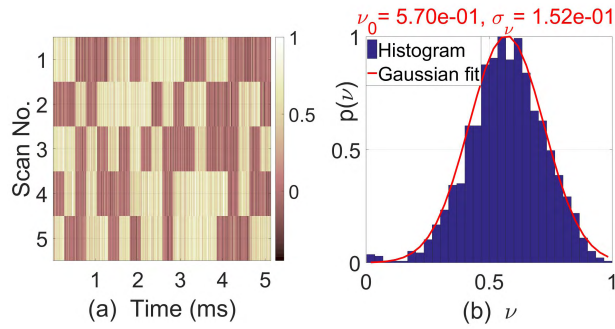


FIGURE 3. (Simulation result) (a) Estimates of tip-sample interaction $\hat{\nu}$; $\hat{\nu}$ is normalized with respect to the maximum obtained value. (b) The probability distribution of ν obtained from simulation. The y axis is normalized with respect to the maximum value of the distribution. The histogram is fit with a Gaussian distribution with mean ν_0 and standard deviation σ_ν .

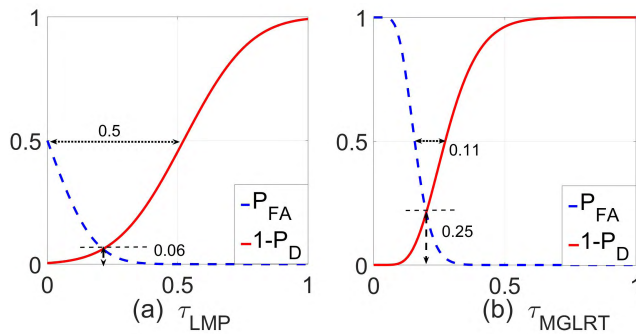


FIGURE 4. (Simulation result) The probability of false alarm P_{FA} and missed detection $1 - P_D$ as functions of decision threshold for (a) LMP technique and (b) for MGLRT scheme. The x axes are normalized with respect to the maximum likelihood ratios obtained from simulation.

The pdf $p(\nu) \sim \mathcal{N}(\nu_0, \sigma_\nu^2)$ is utilized for determining the false alarm rate P_{FA} using (11) and probability of missed detection $1 - P_D$ using (12) for LMP detection technique. Similarly, false alarm and detection probabilities for GLRT and MGLRT methods are evaluated using the set of equations (15), (16), (19) and (21). False alarm rate and probability of missed detection with varying decision thresholds for LMP and MGLRT methods are shown in Fig. 4 (a) and Fig. 4 (b) respectively. From Fig. 4, it is clear that selection of threshold controls the balance between false alarm rate and probability of missed detection. Further, the detection performance of LMP, MGLRT and GLRT schemes are also characterized by the probability of detection as function of the false alarm probability which are shown in Fig. 5.

For LMP detection strategy, it is theoretically possible to simultaneously achieve small P_{FA} and $1 - P_D$ of the value 0.06 (see Fig. 4 (a)). However, in Fig. 4 (b), the best possible scenario for MGLRT with is $P_{FA} = 1 - P_D = 0.25$. The transitions of the false alarm and missed detection rates with respect to changing threshold are more drastic in MGLRT than LMP scheme. From Fig. 4 (a), the range of threshold τ_{LMP} where both P_{FA} and $1 - P_D$ are retained within 0.5 is 0.5. In contrast, in Fig. 4 (b), both P_{FA} and $1 - P_D$ remain below the limit 0.5 only over a narrow range of τ_{MGLRT} which is 0.11.

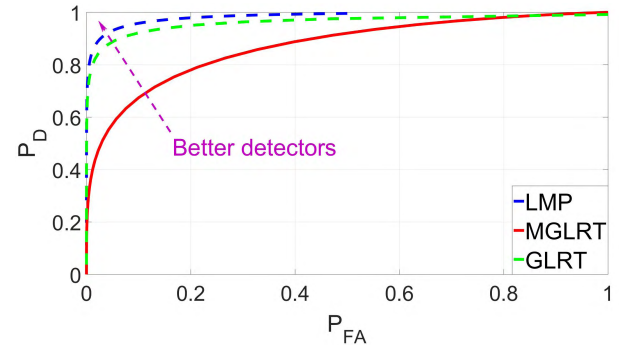


FIGURE 5. (Simulation result) The probability of detection P_D as function of the false alarm probability P_{FA} for LMP, MGLRT and GLRT techniques. Theoretically, LMP scheme is capable of better detection performance than GLRT and MGLRT.

Thus it is evident that LMP imaging performance is less sensitive to selection of threshold compared to MGLRT. Fig. 5 also suggests that theoretically, the LMP technique is capable of achieving the best balance of false alarm and missed detection rates than MGLRT as well as GLRT schemes.

However, synthesizing the LMP likelihood signal $l_{lmp} = e^T V^{-1} \Gamma$ as well as GLRT signal $l_{glrt} = e^T V_{\Gamma, glrt} e$ requires synchronization of the Γ vector precisely with the observation vector e during each decision window. For practical AFM systems, it is difficult to accurately know the timing instants when the oscillating cantilever interacts with the substrate. Another assumption for LMP and GLRT methods which needs to be satisfied is that the estimated models in (3) and (6) are accurate and there are no uncertainties in evaluating Γ in the hypothesis testing framework (9). Since MGLRT scheme alleviates such sensitivity with respect to model uncertainties and timing synchronization by utilizing simple likelihood signal $l_m = e^T e$, it is easy to implement in practical settings, yet it produces reasonable performance as shown later in experimental results.

The effect of selection of decision threshold on fidelity imaging is demonstrated now. Fidelity metrics for MGLRT method are determined using the techniques demonstrated in Theorem 1. Define $\tau_{p, MGLRT}$ as the decision threshold where P_{FA} and $1 - P_D$ are simultaneously minimized to 0.25 as shown in Fig. 4 (b). Fig. 6 (a) and Fig. 6 (b) demonstrate selection of high threshold ($\tau_{MGLRT} = 3\tau_{p, MGLRT}$) on MGLRT decision image and corresponding fidelity image. It is observed in Fig. 6 (a) that the low topography regions are deciphered correctly but in many locations corresponding to high topography zones, dark spots appear which are *missed detections*. The corresponding fidelity image in Fig. 6 (b) demonstrates that there exists higher confidence on the decisions corresponding to low topography zones. However dark lines in fidelity image appear in Fig. 6 (b) corresponding to the missed detection locations (compare with Fig. 6 (a)) indicating that these decisions (which are incorrect) should be given less confidence. The effect of choosing low threshold ($\tau_{MGLRT} = 0.7\tau_{p, MGLRT}$) is demonstrated in Fig. 6 (c) and Fig. 6 (d). In Fig. 6 (c), the high topography regions are

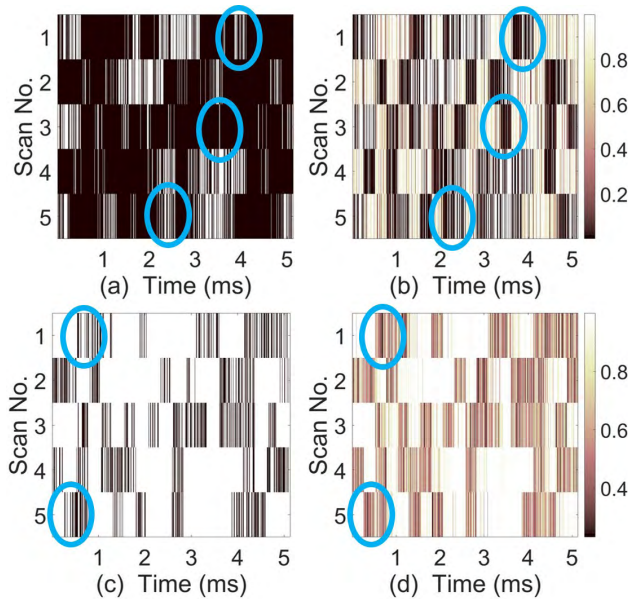


FIGURE 6. (Simulation result) (a) MGLRT decision image and (b) corresponding fidelity image for high threshold. The encircled regions include examples of missed detection. (c) MGLRT decision image and (d) corresponding fidelity image for low threshold. Examples of false alarm are included in the encircled regions. The color bars specify the ranges.

correctly detected, however, bright regions appear in the low topography regions indicating that these locations are *false alarms*. The corresponding fidelity image shown in Fig. 6 (d) assigns low confidence on the pixels that are false alarms. Similar trends in decision images and their fidelity measures can be observed for LMP and GLRT techniques as well.

V. EXPERIMENTAL RESULTS

Results from experiment are presented here. A cantilever with first mode resonant frequency 71.7 kHz and quality factor 127.3 is excited near resonance (drive frequency of 71.8 kHz) for dynamic mode of operation. A freshly cleaved mica substrate is actuated in the vertical direction with the help of an FPGA based actuator circuit. The vertical movement of the mica substrate follows a pseudo-random bit pattern of duration 350 micro seconds. During the high position of the substrate, the oscillating cantilever interacts with mica, while during low position, the cantilever oscillates freely. Fig. 7 (a) shows a typical example of the height profile of the mica substrate. The horizontal axis represents time in milliseconds and the vertical axis represents example runs which are also referred to as the number of scan. The bright (dark) zones represent high (low) position of mica in Fig. 7 (a). The LMP, MGLRT and GLRT images are generated which are demonstrated in Fig. 7 (b), (c) and (d) respectively. The color bars in Fig. 7 (b), (c) and (d) represent the likelihood signals normalized with respect to the corresponding maximum values obtained from experiment.

Based on the knowledge of the discrete time cantilever dynamics (represented by matrices (F, G, H) as shown in (4))

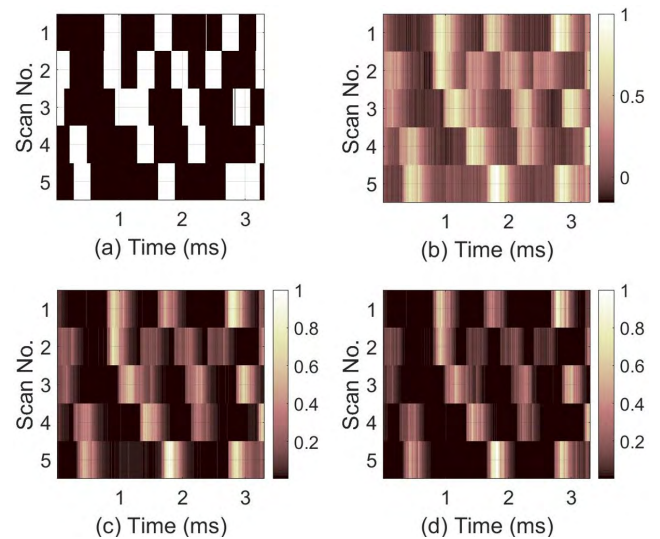


FIGURE 7. (Experimental data) (a) Height image for mica substrate. The bright areas represent raised positions while the dark spots belong to depressed positions. (b) The LMP likelihood, (c) MGLRT likelihood and (d) GLRT likelihood images. LMP, MGLRT and GLRT images are normalized with respect to their maximum values obtained while imaging. The color bars specify corresponding ranges. x axes represent time in milliseconds and y axes represent the number of scan.

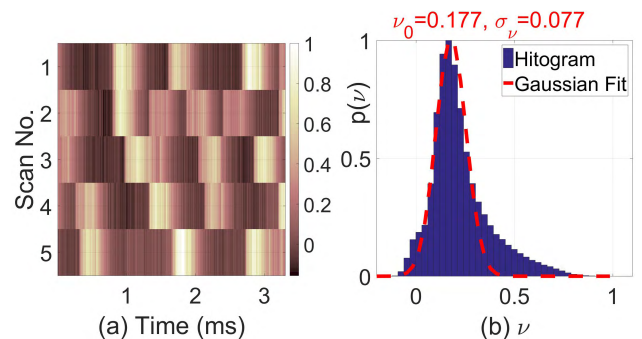


FIGURE 8. (Experimental data) (a) The estimates of tip-sample interactions \hat{v} . The color bar indicates its range. (b) Estimated distribution of the strength of tip-sample interaction, $p(v)$. The histogram is fit with a Gaussian distribution of mean $\nu_0 = 0.177$ and standard deviation $\sigma_\nu = 0.077$.

and the Kalman observer gain, L , the parameter Γ in (8) for the hypothesis testing framework is derived using (9). Subsequently, the error signal, e , generated by the Kalman observer in (5) is processed to estimate the tip-sample interactive forces, \hat{v} , by utilizing the least square estimator in (33). The image for \hat{v} after being normalized with respect to its maximum value is shown in Fig. 8 (a). The estimates shown in Fig. 8 (a) are arranged in histogram to acquire the underlying distribution, $p(v)$, which is shown in Fig. 8 (b). Though there exists a longer tail of the estimated distribution, $p(v)$, extending to the right hand side (see Fig. 8 (b)), the significant population of $p(v)$ (83 percent) is centered around a peak value, which for practical purposes can be approximated utilizing a Gaussian fit (see Fig. 8 (b)) of mean $\nu_0 = 0.177$ and standard deviation $\sigma_\nu = 0.077$. This observation

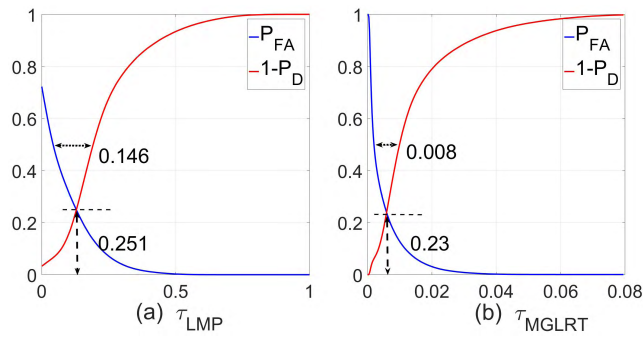


FIGURE 9. (Experimental data) The false alarm rate P_{FA} and probability of missed detection $1 - P_D$ as functions of decision threshold for (a) the LMP method and (b) the MGLRT method. The decision thresholds are normalized with respect to the maximum values of corresponding likelihood signals received from experiment.

experimentally verifies that for approximate calculations, it is reasonable to assume that $p(v) \sim \mathcal{N}(v_0, \sigma_v^2)$.

The likelihood signal images, for example, the LMP and MGLRT images demonstrated in Fig. 7 (b) and Fig. 7 (c) respectively are compared with varying thresholds (denoted by τ_{LMP} and τ_{MGLRT} respectively) for decision imaging. The height image of the actuated mica substrate (as shown in Fig. 7 (a)) is accepted as the true image. Thus a false alarm represents a pixel in the decision image in which the topography is decided to be high (bright zone) whereas in Fig. 7 (a) the same location indicates low topography (dark zone). Similarly a missed detection represents a pixel in the decision image where low topography (dark zone) is decided whereas the same location in Fig. 7 (a) represents high topography (bright zone). Based on this strategy, the false alarm rate P_{FA} and probability of missed detection $1 - P_D$ for LMP and MGLRT images for different choice of decision thresholds are determined which are shown in Fig. 9 (a) and Fig. 9 (b) respectively. The decision thresholds are normalized with respect to the maximum value of likelihood ratios received while imaging. From Fig. 9 (b), it is evident that with MGLRT method it is possible to achieve $P_{FA} = 1 - P_D = 0.23$ for the choice of threshold $\tau_{MGLRT} = 0.0058$. In Fig. 9 (a), the minimum error rate that is achievable with LMP technique is approximately $P_{FA} = 1 - P_D = 0.25$. From Fig. 9 (a), the range of τ_{LMP} over which both P_{FA} and $1 - P_D$ are retained below 0.5 is 0.146. In comparison, in Fig. 9 (b), P_{FA} and $1 - P_D$ stay below the limit 0.5 only over a range 0.008 of τ_{MGLRT} which is less than the range offered by LMP method. Thus, similar to the observations from simulation, the decision accuracy of MGLRT method is found to be more sensitive to the choice of threshold than the LMP method.

In order to compare the receiver operating characteristic for the different detection schemes, instead of displaying P_{FA} and $1 - P_D$ as functions of decision threshold (shown in Fig. 9), P_D is plotted as function of P_{FA} for different detectors in Fig. 10. Interestingly, in Fig. 10 we observe that it is possible to obtain nearly similar trade-off between overall

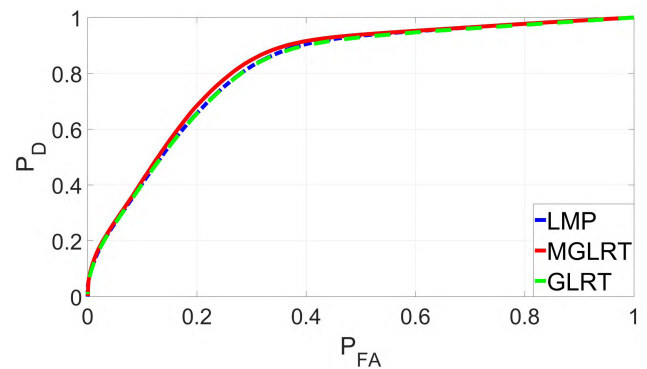


FIGURE 10. (Experimental data) The probability of detection P_D as function of the false alarm rate P_{FA} for the LMP, MGLRT and GLRT methods. Detection performance of different techniques are close match, however, MGLRT is observed to achieve slightly better balance between P_{FA} and P_D .

false alarm and detection performance utilizing the MGLRT method compared to the LMP or GLRT methods. We observed in Fig. 5 that, theoretically, LMP and GLRT methods should offer better detection performance than MGLRT method. Thus in practical situations, LMP and GLRT techniques are losing performance compared to their theoretically achievable limits. This loss of performance for LMP and GLRT techniques compared to the ideal values is hypothesized to be caused by loss of accurate timing information, modeling uncertainties in practical systems, and possibly because of the dependence of tip-sample interactive forces on the history of the topography encountered [27], [44]. We observe from experiments that synthesizing the likelihood signal for the MGLRT technique is more convenient than the LMP and GLRT methods. Due to the simplicity and similar detection characteristics in practical settings, the MGLRT technique is well suited for fidelity imaging. A detailed understanding of the possible strategies to improvise the detection performance of LMP and GLRT methods in presence of the practical challenges mentioned above is left for future research in this study.

The effect of choice of threshold on fidelity imaging is discussed now. Fidelity metrics for MGLRT method are derived using the techniques described in Theorem 1. Fig. 11 (a) and Fig. 11 (b) demonstrate MGLRT decision and fidelity images for a high decision threshold $\tau_{MGLRT} = 2\tau_{p,MGLRT}$ whereas Fig. 11 (c) and Fig. 11 (d) demonstrate effect of relatively lower threshold $\tau_{MGLRT} = 0.25\tau_{p,MGLRT}$; $\tau_{p,MGLRT}$ represents the decision threshold where P_{FA} and $1 - P_D$ are simultaneously minimized to 0.23 as shown in Fig. 9 (b). Consistent with simulation results, high detection thresholds create missed detections in the MGLRT decisions over the raised topographic zones in Fig. 11 (a). The pixels that represent missed detections are assigned low decision confidence in Fig. 11 (b). Putting a relatively lower threshold on the other hand, allows the user to detect most of the high topography zones correctly. However, some low topography zones are falsely interpreted as high topography by the decision image

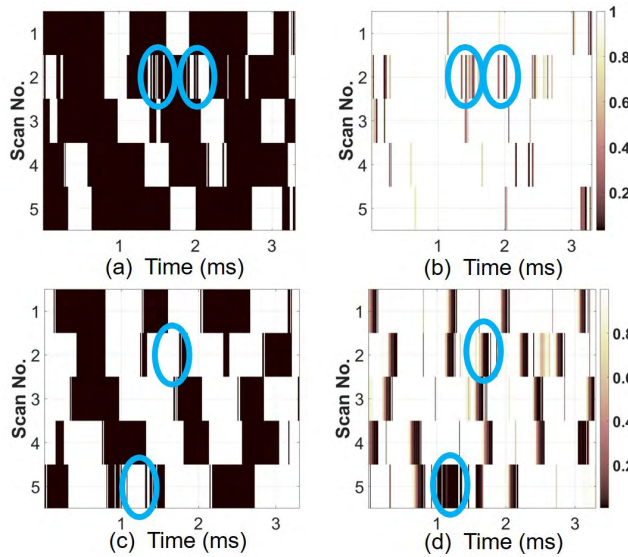


FIGURE 11. (Experimental data) (a) MGLRT decision image and (b) fidelity image for high decision threshold. The encircled regions include examples of missed detection. (c) MGLRT decision image and (d) fidelity image for relatively lower decision threshold. Examples of false alarm are included in the encircled regions. The color bars specify corresponding ranges.

(false alarms) which are demonstrated in Fig. 11 (c). Corresponding fidelity image in Fig. 11 (d) assigns low decision fidelity on the pixels that are false alarms. LMP and GLRT based decision images with associated fidelity images follow similar trend. Thus the fidelity imaging methodology presented in this article is validated extensively by experiments.

VI. CONCLUSIONS

A key challenge in signal detection frameworks which is widely unaddressed in literature is to provide fidelity metrics on the decision data. In this article we developed techniques for providing fidelity measures on some prevalent signal detection algorithms. Fidelity metrics are derived for both the locally most powerful and generalized likelihood ratio test based signal processing techniques. The trade-off between the false alarm rate and probability of detection for the choice of decision threshold is also discussed. Developed methods are demonstrated to be effective for high speed topography imaging using dynamic mode AFM via extensive simulation and experimental results. Demonstrating the effectiveness of fidelity estimates on different applications of signal processing and detection algorithms beyond AFM imaging establishes a natural extension of this work.

REFERENCES

- [1] S. M. Kay, *Fundamentals of Statistical Signal Processing: Practical Algorithm Development*, vol. 3. London, U.K.: Pearson Education, 2013.
- [2] M. Frerking, *Digital Signal Processing in Communications Systems*. New York, NY, USA: Springer, 2013.
- [3] R. W. Heath, Jr., N. González-Prelcic, S. Rangan, W. Roh, and A. M. Sayeed, "An overview of signal processing techniques for millimeter wave MIMO systems," *IEEE J. Sel. Topics Signal Process.*, vol. 10, no. 3, pp. 436–453, Apr. 2016.
- [4] C.-X. Wang *et al.*, "Cellular architecture and key technologies for 5G wireless communication networks," *IEEE Commun. Mag.*, vol. 52, no. 2, pp. 122–130, Feb. 2014.
- [5] S. Furui, *Digital Speech Processing: Synthesis, and Recognition* (Signal Processing and Communications), 2nd ed. Boca Raton, FL, USA: CRC Press, 2000.
- [6] B. Gold, N. Morgan, and D. Ellis, *Speech and Audio Signal Processing: Processing and Perception of Speech and Music*. Hoboken, NJ, USA: Wiley, 2011.
- [7] S. O. Sadjadi and J. H. L. Hansen, "Unsupervised speech activity detection using voicing measures and perceptual spectral flux," *IEEE Signal Process. Lett.*, vol. 20, no. 3, pp. 197–200, Mar. 2013.
- [8] D. Manolakis and G. S. Shaw, "Detection algorithms for hyperspectral imaging applications," *IEEE Signal Process. Mag.*, vol. 19, no. 1, pp. 29–43, Jan. 2002.
- [9] D. Manolakis, E. Truslow, M. Pieper, T. Cooley, and M. Brueggeman, "Detection algorithms in hyperspectral imaging systems: An overview of practical algorithms," *IEEE Signal Process. Mag.*, vol. 31, no. 1, pp. 24–33, Jan. 2014.
- [10] M. Sonka, V. Hlavac, and R. Boyle, *Image Processing, Analysis and Machine Vision*. Boston, MA, USA: Cengage Learning, 2014.
- [11] J. Li, L. Liu, Z. Zeng, and F. Liu, "Advanced signal processing for vital sign extraction with applications in UWB radar detection of trapped victims in complex environments," *IEEE J. Sel. Topics Appl. Earth Observ. Remote Sens.*, vol. 7, no. 3, pp. 783–791, Mar. 2014.
- [12] S. Sanei and J. A. Chambers, *EEG Signal Processing*. Hoboken, NJ, USA: Wiley, 2013.
- [13] H.-H. Chang and J. M. Moura, "Biomedical signal processing," in *Biomedical Engineering and Design Handbook*, vol. 2. New York, NY, USA: McGraw-Hill, 2010, pp. 559–579.
- [14] M. Pieper, D. Manolakis, E. Truslow, T. Cooley, and S. Lipson, "Performance evaluation of cluster-based hyperspectral target detection algorithms," in *Proc. 19th IEEE Int. Conf. Image Process. (ICIP)*, Sep./Oct. 2012, pp. 2669–2672.
- [15] S.-C. Huang, "An advanced motion detection algorithm with video quality analysis for video surveillance systems," *IEEE Trans. Circuits Syst. Video Technol.*, vol. 21, no. 1, pp. 1–14, Jan. 2011.
- [16] N. Ravanshad, H. Rezaee-Dehsorkh, R. Lotfi, and Y. Lian, "A level-crossing based QRS-detection algorithm for wearable ECG sensors," *IEEE J. Biomed. Health Informat.*, vol. 18, no. 1, pp. 183–192, Jan. 2014.
- [17] O. Aziz and S. N. Robinovitch, "An analysis of the accuracy of wearable sensors for classifying the causes of falls in humans," *IEEE Trans. Neural Syst. Rehabil. Eng.*, vol. 19, no. 6, pp. 670–676, Dec. 2011.
- [18] S. C. Mukhopadhyay, "Wearable sensors for human activity monitoring: A review," *IEEE Sensors J.*, vol. 15, no. 3, pp. 1321–1330, Mar. 2015.
- [19] M. G. Amin, Y. D. Zhang, F. Ahmad, and K. C. D. Ho, "Radar signal processing for elderly fall detection: The future for in-home monitoring," *IEEE Signal Process. Mag.*, vol. 33, no. 2, pp. 71–80, Mar. 2016.
- [20] L. Fan, X. Lei, N. Yang, T. Q. Duong, and G. K. Karagiannidis, "Secure multiple amplify-and-forward relaying with cochannel interference," *IEEE J. Sel. Topics Signal Process.*, vol. 10, no. 8, pp. 1494–1505, Dec. 2016.
- [21] L. Fan, X. Lei, N. Yang, T. Q. Duong, and G. K. Karagiannidis, "Secrecy cooperative networks with outdated relay selection over correlated fading channels," *IEEE Trans. Veh. Technol.*, vol. 66, no. 8, pp. 7599–7603, Aug. 2017.
- [22] X. Lai, J. Xia, M. Tang, H. Zhang, and J. Zhao, "Cache-aided multiuser cognitive relay networks with outdated channel state information," *IEEE Access*, vol. 6, pp. 21879–21887, 2018.
- [23] J. Xia *et al.*, "Cache aided decode-and-forward relaying networks: From the spatial view," *Wireless Commun. Mobile Comput.*, vol. 2018, Apr. 2018, Art. no. 5963584.
- [24] F. Shi, L. Fan, X. Liu, Z. Na, and Y. Liu, "Probabilistic caching placement in the presence of multiple eavesdroppers," *Wireless Commun. Mobile Comput.*, vol. 2018, May 2018, Art. no. 2104162.
- [25] G. Binnig, C. F. Quate, and C. Gerber, "Atomic force microscope," *Phys. Rev. Lett.*, vol. 56, pp. 930–933, Mar. 1986.
- [26] L. Gross, F. Mohn, N. Moll, P. Liljeroth, and G. Meyer, "The chemical structure of a molecule resolved by atomic force microscopy," *Science*, vol. 325, no. 5944, pp. 1110–1114, 2009.
- [27] S. Ghosal, G. Saraswat, and M. Salapaka, "Model detection with application to probe based data storage," *Automatica*, vol. 74, pp. 171–182, Dec. 2016.

- [28] C. D. Wright, M. M. Aziz, P. Shah, and L. Wang, "Scanning probe memories—Technology and applications," *Current Appl. Phys.*, vol. 11, no. 2, pp. e104–e109, 2011.
- [29] T. Ando, "High-speed atomic force microscopy coming of age," *Nanotechnology*, vol. 23, no. 6, p. 062001, 2012.
- [30] S. Ghosal, A. Gannepalli, and M. Salapaka, "Toward quantitative estimation of material properties with dynamic mode atomic force microscopy: A comparative study," *Nanotechnology*, vol. 28, no. 32, p. 325703, 2017.
- [31] S. Ghosal, S. Pradhan, and M. Salapaka, "Note: Design of FPGA based system identification module with application to atomic force microscopy," *Rev. Sci. Instrum.*, vol. 89, no. 5, p. 056103, 2018.
- [32] R. Garcia and E. T. Herruzo, "The emergence of multifrequency force microscopy," *Nature Nanotechnol.*, vol. 7, no. 4, pp. 217–226, Apr. 2012.
- [33] A. Gannepalli, D. G. Yablon, A. H. Tsou, and R. Proksch, "Mapping nanoscale elasticity and dissipation using dual frequency contact resonance AFM," *Nanotechnology*, vol. 22, no. 35, p. 355705, 2011.
- [34] A. U. Kareem and S. D. Solares, "Characterization of surface stiffness and probe-sample dissipation using the band excitation method of atomic force microscopy: A numerical analysis," *Nanotechnology*, vol. 23, no. 1, p. 015706, 2011.
- [35] E. M. Puchner and H. E. Gaub, "Force and function: Probing proteins with AFM-based force spectroscopy," *Current Opinion Struct. Biol.*, vol. 19, no. 5, pp. 605–614, 2009.
- [36] F. Rico, L. Gonzalez, I. Casuso, M. Puig-Vidal, and S. Scheuring, "High-speed force spectroscopy unfolds titin at the velocity of molecular dynamics simulations," *Science*, vol. 342, no. 6159, pp. 741–743, 2013.
- [37] G. Haugstad, *Atomic Force Microscopy: Understanding Basic Modes and Advanced Applications*. Hoboken, NJ, USA: Wiley, 2012.
- [38] M. T. Bray, S. H. Cohen, and M. L. Lightbody, *Atomic Force Microscopy/Scanning Tunneling Microscopy*. Boston, MA, USA: Springer, 2013.
- [39] B. Gotsmann and M. A. Lantz, "Atomistic wear in a single asperity sliding contact," *Phys. Rev. Lett.*, vol. 101, no. 12, p. 125501, 2008.
- [40] Q. Zhong, D. Inniss, K. Kjoller, and V. B. Elings, "Fractured polymer/silica fiber surface studied by tapping mode atomic force microscopy," *Surf. Sci.*, vol. 290, nos. 1–2, pp. L688–L692, 1993.
- [41] S. M. Salapaka, A. Ramamoorthy, and M. V. Salapaka, "AFM imaging? Reliable or not?: Validation and verification of images in atomic force microscopy," *IEEE Control Syst. Mag.*, vol. 33, no. 6, pp. 106–118, Dec. 2013.
- [42] R. Garcia and R. Perez, "Dynamic atomic force microscopy methods," *Surf. Sci. Rep.*, vol. 47, nos. 6–8, pp. 197–301, 2002.
- [43] M. E. McConney, S. Singamaneni, and V. V. Tsukruk, "Probing soft matter with the atomic force microscopies: Imaging and force spectroscopy," *Polym. Rev.*, vol. 50, no. 3, pp. 235–286, 2010.
- [44] S. Ghosal, G. Sarawat, A. Ramamoorthy, and M. Salapaka, "Topography detection using innovations mismatch method for high speed and high density dynamic mode AFM," in *Proc. Amer. Control Conf. (ACC)*, Jun. 2013, pp. 5500–5505.
- [45] S. Ghosal and M. Salapaka, "Fidelity imaging for atomic force microscopy," *Appl. Phys. Lett.*, vol. 106, no. 1, p. 013113, 2015.
- [46] D. Sahoo, P. Agarwal, and M. V. Salapaka, "Transient force atomic force microscopy: A new nano-interrogation method," in *Proc. Amer. Control Conf. (ACC)*, Jul. 2007, pp. 2135–2140.
- [47] A. Sebastian, D. R. Sahoo, and M. V. Salapaka, "An observer based sample detection scheme for atomic force microscopy," in *Proc. 42nd IEEE Conf. Decision Control*, vol. 3, Dec. 2003, pp. 2132–2137.
- [48] D. R. Sahoo, T. De Murti, and M. V. Salapaka, "Observer based imaging methods for atomic force microscopy," in *Proc. 44th IEEE Conf. Decis. Control (CDC-ECC)*, Dec. 2005, pp. 1185–1190.
- [49] T. Kailath, A. H. Sayed, and B. Hassibi, *Linear Estimation*, vol. 1. Upper Saddle River, NJ, USA: Prentice-Hall, 2000.
- [50] D. R. Sahoo, A. Sebastian, and M. V. Salapaka, "Harnessing the transient signals in atomic force microscopy," *Int. J. Robust Nonlinear Control*, vol. 15, no. 16, pp. 805–820, 2005.
- [51] N. Kumar, P. Agarwal, A. Ramamoorthy, and M. V. Salapaka, "Channel modeling and detector design for dynamic mode high density probe storage," in *Proc. 42nd Annu. Conf. Inf. Sci. Syst. (CISS)*, Mar. 2008, pp. 1273–1278.
- [52] N. Kumar, P. Agarwal, A. Ramamoorthy, and M. V. Salapaka, "Maximum-likelihood sequence detector for dynamic mode high density probe storage," *IEEE Trans. Commun.*, vol. 58, no. 6, pp. 1686–1694, Jun. 2010.
- [53] C. F. du Toit, "The numerical computation of Bessel functions of the first and second kind for integer orders and complex arguments," *IEEE Trans. Antennas Propag.*, vol. 38, no. 9, pp. 1341–1349, Sep. 1990.
- [54] R. B. Paris, "High-precision evaluation of the Bessel functions via Hadamard series," *J. Comput. Appl. Math.*, vol. 224, no. 1, pp. 84–100, 2009.
- [55] G. N. Watson, *A Treatise on the Theory of Bessel Functions*. Cambridge, U.K.: Cambridge Univ. Press, 1995.
- [56] D. Borwein, J. M. Borwein, and O.-Y. Chan, "The evaluation of Bessel functions via exp-arc integrals," *J. Math. Anal. Appl.*, vol. 341, no. 1, pp. 478–500, 2008.
- [57] A. Sebastian, M. V. Salapaka, D. J. Chen, and J. P. Cleveland, "Harmonic and power balance tools for tapping-mode atomic force microscope," *J. Appl. Phys.*, vol. 89, no. 11, p. 6473, 2001.
- [58] A. Sebastian, A. Gannepalli, and M. V. Salapaka, "A review of the systems approach to the analysis of dynamic-mode atomic force microscopy," *IEEE Trans. Control Syst. Technol.*, vol. 15, no. 5, pp. 952–959, Sep. 2007.
- [59] AC240TS Cantilevers, Asylum Research Probe Store. Accessed: Sep. 5, 2018. [Online]. Available: <https://afmprobes.asylumresearch.com/ac240ts-r3.html>
- [60] G. F. Franklin, J. D. Powell, and M. L. Workman, *Digital Control of Dynamic Systems*, vol. 3, 3rd ed. Menlo Park, CA, USA: Addison-Wesley, 1998.
- [61] B. D. Anderson and J. B. Moore, *Optimal Filtering*. New York, NY, USA: Dover, 2012.



SAYAN GHOSAL (M'17) received the B.E. degree in electronics and telecommunication engineering from Jadavpur University, Kolkata, India, in 2007, the master's degree in communication systems from IIT Madras, Chennai, India, in 2010, and the Ph.D. degree from the Department of Electrical and Computer Engineering, University of Minnesota, Minneapolis, MN, USA, in 2017.

From 2010 to 2016, he was a Graduate Assistant with the Nano Dynamics Systems Laboratory (Renamed as Salapaka Laboratory in 2017) where his research focus included areas of signal processing, control algorithms, machine learning, and FPGA-based embedded systems with application to nanotechnology. Since 2017, he has been with Seagate Technology, as a Lead Engineer in integration, testing, and development of partial response maximum likelihood channels utilized in magnetic data storage systems.



MURTI SALAPAKA (SM'01) received the B.Tech. degree in mechanical engineering from IIT Madras, India, in 1991, and the master's and Ph.D. degrees from the University of California at Santa Barbara, Santa Barbara, CA, USA, in 1993 and 1997, respectively.

He was with the Electrical Engineering Department, Iowa State University, USA, from 1997 to 2007. He is currently a Faculty at the Electrical and Computer Engineering Department, University of Minnesota, Minneapolis, MN, USA. His research interests include span control science and its associated areas of learning, optimization, network theory, and system science. He was a recipient of the NSF CAREER Award and the ISU-young Engineering Faculty Research Award in 1998 and 2001, respectively. His research laboratory (Salapaka Laboratory) has made contributions to different threads of theoretical research including learning structure from measured data in networks with feedback, structured control, multi-objective control synthesis, and distributed computation over networked systems.

...